

# Diffusion and transformation kinetics of small Helium clusters in bulk Tungsten.

Danny Perez\* and Thomas Vogel

*Theoretical Division T-1, Los Alamos National Laboratory, Los Alamos, New Mexico 87545, USA*

Blas P. Uberuaga

*Materials Science and Technology MST-8, Los Alamos National Laboratory, Los Alamos, New Mexico 87545, USA*

(Dated: June 24, 2014)

The production of energy through nuclear fusion poses serious challenges related to the stability and performance of materials in extreme conditions. In particular, the constant bombardment of the walls of the reactor with high doses of He ions is known to lead to deleterious changes in their microstructures. These changes follow from the aggregation of He into bubbles that can grow and blister, potentially leading to the contamination of the plasma, or to the degradation of their mechanical properties. We computationally study the behavior of small clusters of He atoms in W in conditions relevant to fusion energy production. Using a wide range of techniques, we investigate the thermodynamics of the clusters and their kinetics in terms of diffusivity, growth, and breakup, as well as mutation into nano-bubbles. Our study provides the essential ingredients to model the early stages of He exposure leading up to the nucleation of He bubbles.

## I. INTRODUCTION

One of the primary challenges in the development of fusion energy sources is related to materials stability and performance. The materials in a fusion reactor such as ITER experience extreme environments, primarily the interaction with the plasma and damage by fusion neutrons. In particular, the plasma bombards the first wall materials with high doses of He ions which cause significant restructuring and evolution of the material. While the incident energy of the ions is modest ( $\sim 50$  eV), they can still penetrate a few nm into the materials and subsequently diffuse into the bulk. In these plasma facing materials, for which tungsten is a leading candidate<sup>1,2</sup>, this He intake leads to the formation of features such as He blisters<sup>3</sup> and so-called fuzz, a micron-thick tangle of nm-thick tungsten whiskers<sup>4-7</sup>. The formation of these features both changes how the surface of the material interacts with the plasma but also leads to the release of tungsten into the plasma, severely disrupting its performance<sup>8</sup>. Thus, there is a strong imperative to both understand and, ultimately, control the evolution of tungsten in the presence of plasmas. This, in turn, requires a detailed understanding of how components of the plasma, such as He, interact with the material at the atomic scale. Note that He is not generated by transmutation reactions<sup>9</sup>, so that its presence in the material can be exclusively attributed to the contact with the plasma.

The evolution of He in metals has been studied for over 50 years and that research has lead to a picture of He evolution that is both complex and intriguing. He, introduced either via implantation in laboratory experiments or via transmutation in reactor applications, diffuses through the lattice, either encountering traps or other He atoms, as there is significant binding between He atoms due to elastic interactions resulting from the repulsion between the He and the metal atoms<sup>10</sup>. Once He clusters grow to a certain size, they can force the emission of interstitials from the cluster, creating vacan-

cies (V) that accommodate the cluster. This so-called trap mutation process was first identified experimentally in 1977 by van Veen, et al., in which they found Kr impurities in W would trap He and lead to the formation of Frenkel pairs<sup>11</sup>. Soon after, in 1981, Wilson, Bisson, and Baskes performed molecular dynamics simulations of He in Ni in which they directly observed this trap mutation process, though they dubbed it self-trapping<sup>12</sup>. As the He-V clusters accumulate more He, forming proper bubbles, they grow via the continual emission of interstitials and, as they grow larger, interstitial loops. This loop punching mechanism was first described in 1959 as a mechanism by which silver precipitates in silver halides released strain as they grew<sup>13</sup> and discussed first in the context of He bubbles by Greenwood, Foreman and Rimmer that same year<sup>14</sup>. Trap mutation and loop punching formed the basis of a model of He bubble nucleation and growth proposed by Baskes and coworkers<sup>15,16</sup>, in which they concluded that such mechanisms were responsible for the complex retention behavior of He in metals. The ability of He clusters and bubbles to grow via trap mutation-like processes has several important implications. First, He bubbles can nucleate and grow under conditions where vacancy mobility is essentially non-existent<sup>17</sup>. Second, this growth is insaturable, meaning a “single” trap site can accommodate a limitless number of He atoms<sup>18</sup>. Third, He thus drives the generation of vacancies and interstitials within the material<sup>19-21</sup>.

Since these early studies, a large body of work, both experimental and theoretical, has focused on the migration of He and the nucleation and growth of small He clusters and bubbles in metals. Here, we summarize some of the key results for He behavior in BCC metals, with a focus on W. In He desorption experiments in Mo, Caspers et al.<sup>22</sup> observed trap mutation of  $\text{He}_N\text{V}$  complexes into  $\text{He}_N\text{V}_2$  complexes for  $N > 6$ . Lhuillier et al. used NRA (Nuclear Reaction Analysis) and PAS (Positron Annihilation Spectroscopy) to show that He bubble formation in W does not require preexisting vacancies but can form

via trap mutation<sup>21</sup>, though radiation-induced vacancies can also serve as nucleation sites for bubbles<sup>20</sup>. Further experimental studies have shown that impurities can trap He in W and ultimately lead to trap mutation processes which nucleate bubbles<sup>11,20,23</sup>. Loop punching from He bubbles has also been observed in experiments on Mo<sup>17</sup> and W<sup>20</sup>.

Atomistic simulations, both using electronic structure calculations and classical potentials, have provided details into these mechanisms. Density functional theory calculations of He in BCC metals have focused on the properties of single He interstitials and small He clusters and complexes. These have identified that He interstitials reside in tetrahedral interstices in Fe and W<sup>10,24</sup>, have very small migration energies (of about 0.06 eV in W)<sup>10,24</sup>, and bind strongly with impurities in Fe<sup>25,26</sup>. Simulations using potentials have examined larger agglomerates of He, including the behavior of He bubbles, within metallic matrices. They have confirmed that trap mutation is a mechanism for He bubble nucleation in Fe<sup>27-30</sup> and W<sup>31,32</sup> and that loop punching is indeed a mechanism for He bubble growth in Fe<sup>30,33,34</sup>, Mo<sup>35</sup> and W<sup>31,32,36</sup>. Simulations have also shown that H aids in the loop punching of He bubbles<sup>37</sup>. Many of these observations extend to other metals as well, as reviewed by Trinkaus<sup>38</sup>.

These atomistic simulations provide the detail necessary to parameterize higher level models of He bubble evolution within materials, which can be applied in kinetic Monte Carlo<sup>39-41</sup>, rate theory<sup>16,42</sup>, and cluster dynamics<sup>43</sup>, for example. However, typically, not all of the relevant thermodynamic and kinetic properties are available, especially regarding the rates at which He interstitial clusters diffuse and transform into other complexes. While migration energies and prefactors have been determined for He interstitial clusters in Fe<sup>29</sup>, systematic studies of He interstitial cluster behavior have not been reported for He in W. The goal of the present work is to determine the relevant thermodynamic and kinetic parameters that describe He in W to inform higher level models. The current study is concerned with the behavior of He in bulk W, an environment that is typical of the nucleation and initial evolution of extended He defects, as the interaction of small clusters with the surface is very short ranged<sup>44</sup>.

The paper is organized as follows: the different simulations techniques used in this work are described in Sec. II, the structure and thermodynamics of He clusters are discussed in Sec. III A, while their diffusion, breakup, and mutation kinetics are investigated in Secs. III B, III C and III D, respectively; finally, implications for the parameterization of cluster dynamics models are discussed in Sec. IV, before concluding.

## II. METHODS

Simulations were carried out using different atomistic simulations methodologies, namely conventional Molecular Dynamics (MD), Temperature Accelerated Dynamics (TAD)<sup>45</sup>, and statistical temperature (STMD)<sup>46</sup> and multicanonical Molecular Dynamics<sup>47,48</sup>. TAD is an accelerated MD technique<sup>49</sup> that allows for an extension of the timescale amenable to simulations in cases where the dynamics are activated, i.e., where evolution occurs through a sequence of rare structural transitions separated by relatively long periods of strictly vibrational motion. TAD proceeds by running simulations at elevated temperatures to speedup the occurrence of rare transitions, and by filtering these possible transitions to select those that are statistically appropriate for evolution at a lower temperature. The end result is that the dynamics can be significantly accelerated when barriers are sufficiently high. For details, the readers are referred to the original publication<sup>45</sup>. A useful side-effect of TAD is that all possible transition are fully analyzed by the means of a Nudged Elastic Band (NEB)<sup>50</sup>. This in turn enables one to easily characterize available transition pathways. A subset of the MD simulations were also fully analyzed using the NEB method, i.e., every 100 fs, the trajectory was interrupted to determine whether a transition occurred. If it did, a NEB was used to identify the pathway connecting the previous and current states. In that case, all states and saddles points were also saved and analyzed.

The thermodynamics of this system were investigated using multicanonical MD<sup>47,48</sup>, a generalized-ensemble method where one aims at performing a random walk in a collective variable, in our case the internal energy  $E$ . In practice, this is done by reweighting the interatomic forces during a conventional canonical simulation at a reference (thermostat) temperature  $T_0$  via

$$f_{\text{muca}} = \frac{T_0}{T(E)} f_{\text{can}}. \quad (1)$$

Here  $T^{-1}(E) = \partial S(E)/\partial E$ , with  $S(E)$  being the microcanonical entropy which is related to the density of states  $g(E)$ .  $T(E)$  is iteratively obtained via the STMD approach<sup>46</sup>. In that scheme, one begins with a constant initial 'guess'  $T_{t=0}(E) = T_0$  (corresponding to conventional canonical MD at  $T_0$ ) and updates the estimator  $T_t(E)$  at every time  $t$  by effectively accumulating a bias potential, as also done in metadynamics, cf. Ref. 48. Once  $T_t(E)$  is converged, we record histograms  $H(E, Q)$  of the internal energy and other observables of interest  $Q$ . Those histograms can then be reweighted to any other ensemble and observable averages can be calculated at any temperature in the range initially covered by the estimator for  $T(E)$ .

Calculations were carried out using an Embedded Atom Method (EAM) description of the interatomic interactions, with W-W interactions from Ackland and

Thetford<sup>51</sup> and modified by Juslin and Wirth<sup>52</sup>, He–He interactions from Beck<sup>53</sup> and modified by Morishita et al.<sup>54</sup>, and He–W interactions from Juslin and Wirth<sup>52</sup>. The simulation cells contained  $6 \times 6 \times 6$  W unit cells, for a total of 432 W atoms. The small size of the cell is instrumental in reaching the long timescales necessary to characterize the dynamics at low temperatures, or for high barrier events. We verified that this size was adequate to properly capture the energetics of the clusters. For example, for  $N = 6$ , we only observe a 0.3% decrease in the energy of a cluster (compared to the perfect W bulk) by increasing the cell size by a factor of 2 in every direction. He atoms are added as appropriate. We investigated  $\text{He}_N$  clusters from  $N = 2$  to 7 at temperatures covering the whole range of relevance to fusion applications, which is centered around 1000 K. All He atoms are interstitial at the beginning of the simulations.

### III. RESULTS

We are interested in three primary aspects of the kinetics of He clusters in tungsten: diffusion, breakup into smaller clusters, and “trap mutation” (i.e., conversion from an interstitial to a substitutional cluster through the creation of a W Frenkel pair). These three mechanisms control the microstructural impact of He on the tungsten wall. Each will be discussed in turn in the following sections.

#### A. Structure and Thermodynamics

We first used TAD to identify the dominant low-temperature pathways (i.e., the ones with the lowest energy barrier). This was done by running TAD with a relatively low target temperature of 300 K (in order to maximize the likelihood of finding the lowest-barrier pathway) and a high temperature of 600 K. The duration of each simulation varied, being a function of the typical barriers in the system, but ranged from tens of nanoseconds to tens of microseconds. The simulation cell for each size cluster started with the lowest energy structure of the next lowest size cluster and one addition He interstitial. The trajectory was allowed to evolve until the two species encountered one another, forming a larger interstitial He cluster, and further evolved to allow for diffusion of the cluster. The trajectory was then analyzed to identify both the lowest energy diffusion pathway for each cluster as well as the lowest energy structure for each cluster.

Figure 1 shows the structure of the ground state cluster geometry for clusters of size  $N = 1$  to 6. The structure of the tetrahedral interstices in BCC tungsten are illustrated in Fig. 1a while the idealized structures for the clusters are given in Figs. 1b-g. There are 24 tetrahedral interstices at  $1/2, 1/4, 0$  positions within the BCC unit cell, including those on periodic faces. Octahedral interstices, not shown, reside at  $1/2, 0, 0$  and  $1/2, 1/2, 0$ ; there

are 18 such sites. For nearly all clusters, the ground state structure involves He atoms sitting on tetrahedral interstices within the BCC lattice. The exception is  $N = 5$ , which is discussed below. For the other size clusters, He atoms first arrange themselves along a  $[100]$  direction across the edge of one unit cell ( $N = 2$ ). The structure for  $N = 4$  is two of these pairs lying perpendicular to one another while  $N = 3$  represents an intermediate structure between  $N = 2$  and  $N = 4$ . The structure for  $N = 6$  becomes more complex. In this case, the He atoms all lie within the unit cell. There are still two pairs of  $[100]$  oriented He atoms, but they no longer lie directly opposite one another, as for  $N = 4$ . This is to accommodate the other two He atoms that lie on opposite faces of the unit cell and tend to create a more open structure than the more compact  $N = 4$  structure. As mentioned,  $N = 5$  is the exception in that not all of the He atoms occupy tetrahedral positions. First, four He atoms reside on tetrahedral sites, but break the motif of  $N = 4$ , forming two  $[100]$  pairs which are now oriented parallel to one another. Further, the fifth He atom occupies an octahedral rather than a tetrahedral interstice. This seems to have consequences for the mobility of this cluster, as will be discussed below.

As the size of the cluster increases, so does the strength of the binding of the cluster, as shown in Fig. 2 for cluster sizes  $N = 2$  to 6. Coincident with the change in structural motif discussed above for  $N = 5$ , there is a bend in the  $E_N - NE_1$  curve ( $E_s$  being the energy of a cluster of size  $s$ ) at that size and a local maximum of  $E_N - E_{N-1} - E_1$ .

Finite temperatures could affect the zero-temperature properties described above, which could be particularly important for fusion applications as operating temperatures are very high. We therefore computed free energy differences between different clusters of sizes  $N = 2$  to 6. For this purpose, two He atoms are considered to be part of the same cluster if they are closer than a cutoff distance of 2.8 Å. This is a proper choice, as it contains most of the first peak of the probability distribution function for He–He distance, as shown in Fig. 3 for  $N = 2$  and  $T = 1500$  K. We verified that the results are not significantly affected by the precise choice of the cutoff radius. After obtaining the proper simulation weights  $w_{\text{muca}}(E)$  via individual STMD runs, we perform a multicanonical production run (applying Eq. 1) for every  $N$  and measure the 2-dimensional joint distribution of  $E$  and cluster composition  $Q$ . For  $N = 2$  there can be 2 different compositions (either a cluster consisting of 2 atoms or two single He atoms), for  $N = 3$  there are 3 possible compositions – a cluster of 3 (ooo), a cluster of 2 plus a single atom (o-o), and three single atoms (o-o-o), etc. By reweighting the multicanonical histograms  $H(E, Q)$  we can compute the canonical distributions of cluster compositions at all temperatures  $T$  via

$$P_T^{\text{can}}(Q) = \sum_E w_{\text{muca}}^{-1}(E) H(E, Q) e^{-E/k_B T}, \quad (2)$$

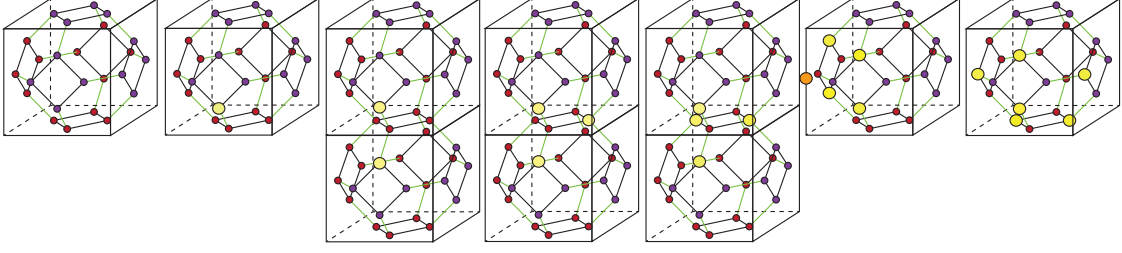


FIG. 1. The lowest energy structure of each cluster for sizes  $N = 1$  to 6. (a) Position of the tetrahedral interstices within the unit cell of the BCC tungsten lattice, adapted from Ref. 55. The colors are simply guides for the eye to distinguish tetrahedral sites on the back faces of the unit cell from the front faces. The black lines connect tetrahedral sites separated by  $1/4, 1/4, 0$  (in units of the lattice constant of the material) on a given face of the unit cell while the green lines connect tetrahedral sites separated by  $1/4, 1/4, 0$  on opposing faces of the unit cell. Tungsten atoms, not shown, reside on the corners and at the body center of the cube. (b-g) Structures of He interstitial clusters from size 1 to 6. The position of each He atom within the cluster is highlighted in yellow when it occupies a tetrahedral site and orange (only for  $N = 5$ ) when it occupies an octahedral site. These are idealized positions within the tetrahedral interstice sublattice. In reality, atomic forces result in some distortion away from these ideal positions upon minimization of the forces.

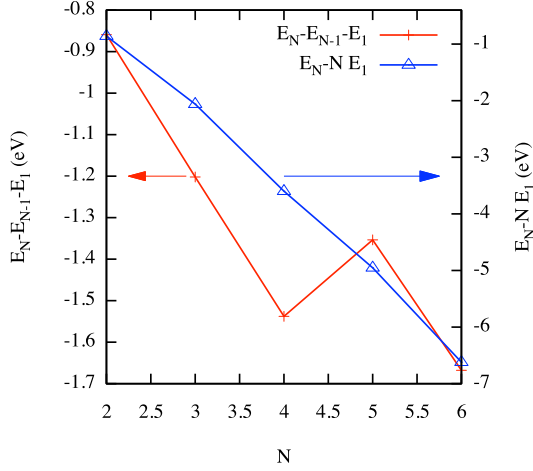


FIG. 2. Energy change (at  $T = 0$  K) upon removal of single atoms from a cluster of size  $N$  ( $E_N - E_{N-1} - E_1$ ; red, left axis) and upon complete fragmentation into  $N$  single atoms ( $E_N - NE_1$ ; blue, right axis).

where the sum extends over all energy bins. From these distributions, one calculates the probabilities  $p_Q(T)$  to find certain cluster compositions  $Q$  at a given temperature. As an example, we plot these probabilities for  $N = 4$  in Fig. 4. For temperatures  $T \lesssim 2500$  K, the most prominent cluster configuration is a single cluster containing all four He atoms. Single atoms start to split off at  $T \approx 1500$  K, though, and most cluster compositions are present by  $T \approx 3000$  K.

While these probabilities depend on the volume of the simulation cell, they can be used to obtain the (volume-independent) free energy of the different clusters. Writing the free energy of a cluster of size  $s$  as  $F_s(T) = -k_B T \ln q_s$ , with  $q_s$  being the partition function of that cluster, the free energy difference for the complete breakup of a cluster of size  $s$  into  $s$  single atoms reads  $F_s - sF_1 = -k_B T \ln(q_s/q_1^s)$ . Analogously, the free energy

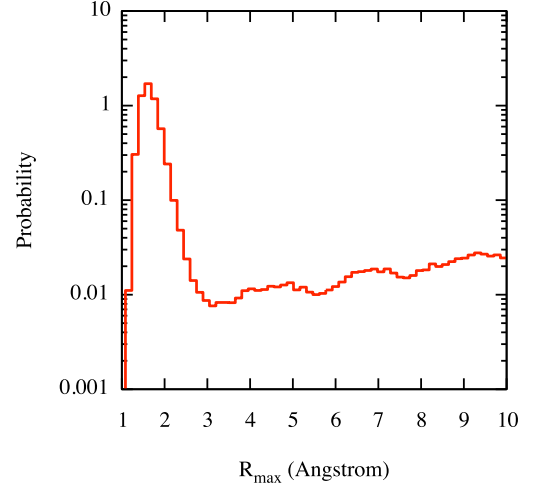


FIG. 3. Probability distribution function of the He-He distance for  $N = 2$  at 1500 K.

change upon the loss of a single atom from a cluster of size  $s$  reads  $F_s - F_{s-1} - F_1 = -k_B T \ln(q_s/q_{s-1}q_1)$ . Based on the formalism developed in Ref. 56, one can show that the above ratios of cluster partition functions are related to ratios of the probabilities  $p_Q(T)$  to find certain cluster compositions. For example,  $q_3/q_2q_1 = p_{(ooo)}/p_{(o-oo)}$ , and  $q_3/q_1^3 = p_{(ooo)}/(3! p_{(o-o-o)})$ , and so on. The corresponding free energy differences are reported in Fig. 5.

At low temperatures, the probabilities of finding single atoms are vanishingly small (see Fig. 4, for example), hence it is almost impossible to accurately calculate the probability ratios. However, the value at  $T = 0$  K can be inferred from the binding energies reported above. The lines in Fig. 5 are fits to the data including those points. We note that even without including those points in the fits, the extrapolation is almost perfect in all cases (not shown). It is therefore unlikely that abrupt changes in the behavior of the free energy occur below 1000 K. It



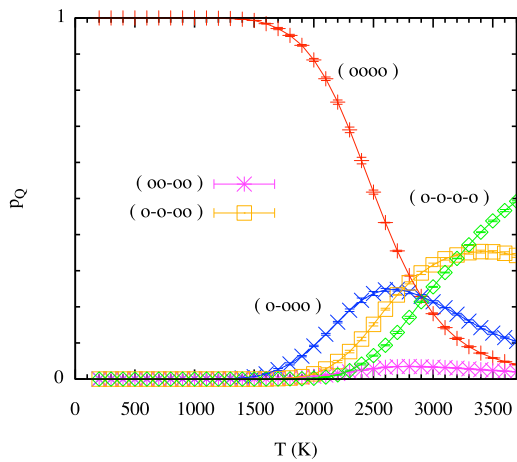


FIG. 4. Probability of finding a certain cluster distribution for  $N = 4$ . See text for details.

can be qualitatively seen that the temperature at which atoms split off the cluster or at which clusters break up completely grows with  $N$ , in accordance with the behavior observed at  $T = 0$  K.

## B. Diffusion

A crucial characteristic of He clusters is how fast they diffuse through the lattice. This quantity controls the timescale on which clusters and bubbles can grow and how far He can penetrate into bulk W. In the following, we discuss the nature of the diffusion pathways for clusters of sizes  $N = 1$  to 6, and then discuss the diffusivity and its temperature dependence, as measured through direct MD simulation.

### 1. Diffusion pathways

Figure 6 shows the lowest energy pathway found for each cluster size. The minimum energy pathway, as identified from the TAD simulations using the NEB method, is given as a function of the reaction coordinate in angstroms. It should be noted that the NEBs were not fully converged all along the path, only the highest energy saddle point for each section of the path was fully converged. However, the rest of the images are close to converged. In several cases, the pathway involves multiple steps that were identified in the TAD simulation as separate events. The pathways in Fig. 6 are a composite of the unique state-to-state events that lead to the migration of the cluster.

For  $N = 1$ , the simplest “cluster”, the diffusion pathway goes from the lowest energy structure, which is the He occupying a tetrahedral interstice in the BCC lattice, through an octahedral interstice, which is the saddle point, to another tetrahedral site. The barrier for this

process is 0.15 eV. This process is essentially the opposite of that found for carbon diffusing within BCC Fe<sup>57</sup>.

As the cluster size increases, the pathways for diffusion become more complex, with more intermediate minima along pathways that describe net translation of the cluster. For example, for  $N = 2$ , there is an intermediate minimum halfway through the diffusion process. This intermediate minimum is relatively deep in energy, only 0.06 eV higher than the lowest energy state. For even larger cluster sizes, there tend to be very shallow minima, or shoulders, on the side of the largest saddle peaks in the minimum energy path. Many of these shallow minima are associated with saddle points that are extremely small, only a few meV in some cases (e.g.  $N = 6$ ). However, along each pathway there are also relatively deep intermediate minima, sometimes almost degenerate in energy with the lowest energy state (e.g.  $N = 3$ ).

Results are summarized in Fig. 7, in which the energy of the highest energy saddle along the lowest energy pathway is given versus the size of the cluster. Initially, as the size of the cluster increases, the barrier increases linearly with the size of the cluster. However, clusters of size 5 exhibit extremely high mobility, which is again reduced significantly for  $N = 6$ . This coincides with the structure of the clusters. Recall that all of the clusters are comprised of He atoms residing on tetrahedral sites with the lone exception of  $N = 5$ . That cluster has one He atom in an octahedral interstice. Interestingly, similar anomalously fast diffusion for He<sub>5</sub> interstitial clusters has been observed in Fe<sup>29</sup>. For  $N = 1$ , the octahedral interstice is the saddle point for migration, indicating that He at the octahedral interstice is less energetically favorable than at the tetrahedral site. This further implies that He mobility might be higher for such a structure, which is reflected in the low migration energy.

### 2. Diffusivity

The diffusivity of the different clusters was directly measured over temperatures ranging from 300 K to 1400 K by computing the mean squared displacement (MSD) of the cluster’s center of mass and using Einstein’s relation

$$D = \lim_{t \rightarrow \infty} \frac{\langle |r(t) - r(0)|^2 \rangle}{2dt}, \quad (3)$$

where  $d$  is the dimension, i.e., 3. In practice, we used 24 independent simulations, totalling about 600 ns of MD time at each temperature. The diffusivity was obtained from a linear fit to the time-dependent MSD. The results are summarized in Fig. 8. At first glance, the most obvious feature is the departure from a conventional Arrhenius [ $D \propto \exp(-\Delta E/k_B T)$ ] behavior. While, at modest temperatures, the change of the diffusivity is compatible with the diffusion barriers identified with TAD (the blue lines are Arrhenius fits using the TAD values of the activation energies), the Arrhenius curves bend downwards

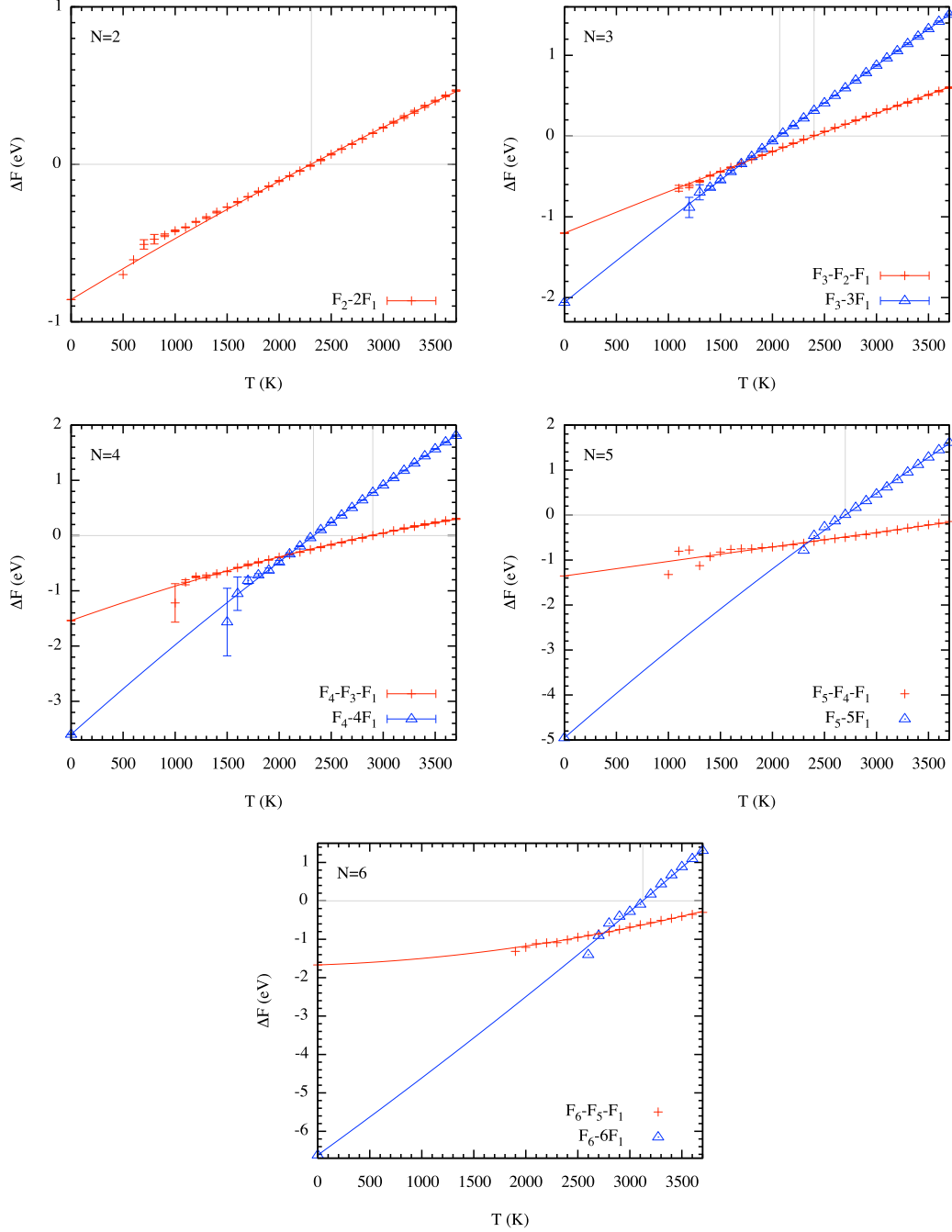


FIG. 5. Free energy change upon removal of single atoms from a cluster of size  $N$  ( $F_N - F_{N-1} - F_1$ ; red) and upon complete fragmentation into  $N$  single atoms ( $F_N - NF_1$ ; blue).

at high temperatures, i.e., diffusion occurs slower than suggested by an extrapolation from lower temperatures. This observation is counter-intuitive because one could have expected that, due to the complexity of the clusters' energy landscape, other, higher energy diffusion pathways would have become active with increasing temperature. This would have led to an opposite, i.e., convex, deviation from the Arrhenius behavior.

The origin of this unexpected behavior indeed stems

from the complexity of the energy landscape. However, not in terms of a multiplicity of diffusion pathways but of possible conformations of the clusters. Consider a case where only one transition pathway is active but where the cluster has to be found in a specific configuration for the hop to be possible. As the temperature varies, the relative probability that the cluster be found in such a "gateway" conformation also varies, which leads to a non-Arrhenius behavior, i.e., to a temperature-dependent

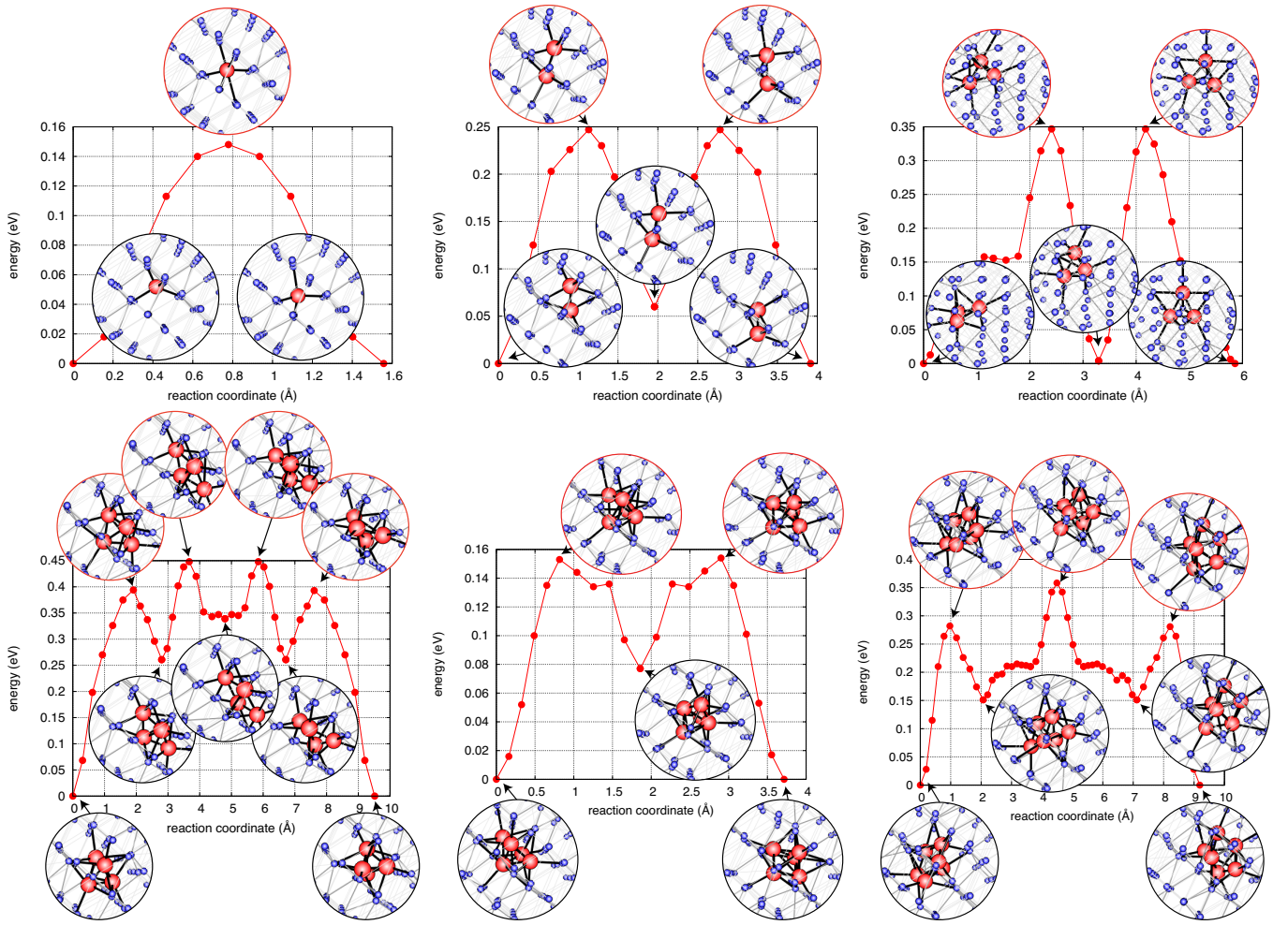


FIG. 6. Lowest energy migration pathway for interstitial He clusters from sizes  $N = 1$  to 6 as identified from TAD simulations. In these figures, the minimum energy path (MEP) is given by the points on the curve. Tungsten atoms are smaller/blue spheres while He atoms are larger/red spheres.

effective activation energy. In fact, an explicit expression for this energy can be derived within the purview of what we term Super-Basin Transition State Theory (SB-HTST):

$$\frac{\partial \ln k/k_0}{\partial \beta} = -[U_G^* - \langle U_{\min} \rangle_{S,\beta}] = -\Delta \tilde{E}(\beta). \quad (4)$$

This expression states that the apparent activation energy (i.e., the slope of the Arrhenius curve) corresponds to the difference between the saddle point energy for diffusion  $U_G^*$  and the average energy of the minima (the different conformations) that the trajectory visits  $\langle U_{\min} \rangle_{S,\beta}$  during dynamics at inverse temperature  $\beta$ . The complete derivation is presented in Annex A. Finally, integrating this expression with respect to  $\beta$ , one can obtain a generalized Arrhenius expression:

$$D = \hat{\nu} \exp(-\beta \Delta \hat{E}), \quad (5)$$

where the generalized activation energy  $\Delta \hat{E}$  is now a

function of temperature, but where the prefactor  $\hat{\nu}$  is temperature independent.

As can be seen from Eq. (4), SB-HTST predicts a lowering of the slope of the Arrhenius curve at increasingly high temperature, due to the fact that higher-lying energy basins are sampled increasingly often, in qualitative agreement with the MD results. Except for a slight under-correction at  $N = 3$ , SB-HTST in fact quantitatively predicts the behavior of the diffusivity, as shown by the green lines in Fig. 8. In this case,  $\langle U_{\min} \rangle_{S,\beta}$  is measured directly from MD simulations by periodically quenching the trajectory and recording the energy of the minima where it was instantaneously located.  $\langle U_{\min} \rangle_{S,\beta}$  was then fitted to a third order polynomial in  $T$ , from which  $\Delta \hat{E} = f_0 + f_2 T^2 + f_3 T^3$  was finally obtained. The value of  $\hat{\nu}$  was here fitted directly to the MD data. The results are presented in Table I. For  $N = 3$ , where the disagreement is the largest, we verified that the MSD is directly proportional to the number of crossings of the diffusion barrier identified by TAD over the whole tem-

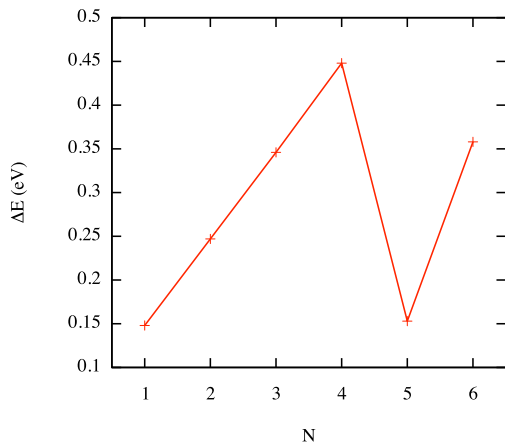


FIG. 7. Migration energies as a function of cluster size for  $N = 1$  to 6.

N	$\hat{\nu}$ ( $\text{m}^2 \text{s}^{-1}$ )	$f_0$ (eV)	$f_2$ ( $\text{eV}/\text{K}^2$ )	$f_3$ ( $\text{eV}/\text{K}^3$ )
2	$3.26 \times 10^{-7}$	0.26	$1.80 \times 10^{-7}$	$-3.79 \times 10^{-11}$
3	$5.61 \times 10^{-7}$	0.35	$8.02 \times 10^{-8}$	$-1.48 \times 10^{-11}$
4	$2.86 \times 10^{-6}$	0.46	$1.98 \times 10^{-7}$	$-3.84 \times 10^{-11}$
5	$1.98 \times 10^{-8}$	0.16	$1.18 \times 10^{-7}$	$-1.30 \times 10^{-11}$
6	$2.32 \times 10^{-6}$	0.375	$4.21 \times 10^{-7}$	$-9.77 \times 10^{-11}$

TABLE I. Parameters of the SB-HTST description of the diffusivity for different cluster sizes. See text for details.

perature range, i.e., no other pathway significantly contributes to diffusion. As SB-HTST is an harmonic theory (i.e., it assumes that the partition functions of each conformation can be approximated by a many-dimensional harmonic partition function), the most likely source of error is anharmonicity of the potential energy surface. Interestingly, for  $N = 1$ , we observe a similar departure from a perfectly Arrhenius behavior. We did not observe any other thermally-relevant configuration of the interstitial that could cause a super-basin correction. Therefore, anharmonicity is probably also the cause of the departure from the Arrhenius behavior in this case.

### C. Breakup

A second key process that controls the size distribution of He clusters is the breakup of larger clusters into smaller ones. Even if clustering is energetically favorable, configurational entropy considerations favor isolated He atoms at low concentrations and high temperatures. Proper consideration of breakup reactions is also essential to model the time and position at which clusters will reach a sufficient size to trap mutate and create a bubble nuclei.

A proper definition of a suitable reaction coordinate to describe the breakup process is essential. Unfortunately, a simple choice based on a cutoff distance be-

tween atoms is not suitable. Indeed, defining breakup (formation) as was done in the thermodynamic analysis above — as the moment at which the minimal distance  $R$  within which every member of the cluster can be connected to some other member of the cluster exceeds (falls below) a certain threshold  $R_{\text{max}}$  — gives an inadequate *kinetic* description. Indeed, an ideal definition should be such that both breakup and (re-)formation of the cluster is approximatively a Markovian process, i.e., that it be well described by a rate constant (in fact, this condition is necessary, e.g., if the dynamics are to be described by a rate theory or a cluster dynamics model). Markovianity in turns implies that the breakup and formation time distribution should be exponential, or, equivalently, that the 1 minus the cumulative reaction time distribution be exponential. The measured distributions for  $N = 2$  and  $T = 1500 \text{ K}$  for  $R_{\text{max}} = 2.8 \text{ \AA}$ , reported in Fig. 9, show that this simple procedure is inadequate because it is associated with an excess of rapid (re-)formation of the cluster, i.e., many “breakups” really correspond to a short-lived fluctuation of the cluster. As  $R_{\text{max}}$  is increased, an excess of short-time pseudo-formation also occur, corresponding to He atoms that came in close proximity, without bonding for a significant amount of time. We found that no single value of  $R_{\text{max}}$  gives satisfactory results. Alternatively, one might consider, following Ref. 58, that the fully bound  $R < R_{\text{bound}}$  and fully unbound  $R > R_{\text{unbound}}$  regions of configuration space are well separated ( $R_{\text{bound}} \neq R_{\text{unbound}}$ ), i.e., that a cluster can temporarily be found in neither the fully bound or fully unbound regions of configuration space, but that its bound/unbound status can still be determined by the last region it visited. In other words, a cluster is bound if it more recently met the condition  $R < R_{\text{bound}}$  than  $R > R_{\text{unbound}}$ , and vice-versa. In this formalism, spurious rapid recrossings of the  $R_{\text{max}}$  surface are not deemed reactions and only unambiguous breakups/formations are counted. The reaction dynamics can therefore be made Markovian to a good approximation, as shown in Fig. 10 for  $R_{\text{bound}} = 2 \text{ \AA}$  and  $R_{\text{unbound}} = 7 \text{ \AA}$ . We find this definition to be adequate for all cluster sizes and temperatures investigated here.

Using this approach, we directly measured the breakup rate of clusters in MD between 1000 and 1500 K. The breakup rates for  $N = 2$  to 5 are shown in Fig. 11. At 1000 K, the lifetime of clusters is on the order of 10 ns, 0.1  $\mu\text{s}$ , 1  $\mu\text{s}$ , and 10  $\mu\text{s}$ , for  $N = 2, 3, 4$ , and 5, respectively. We did not observe breakup for  $N = 6$  on accessible timescales. The results indicate a rapid decrease of the breakup rate with increasing cluster size. As shown in Table II, where the results of Arrhenius fits to the breakup rates are reported, the activation barriers for breakup increase significantly with increasing size, which is consistent with the fact that the binding energy per He atom increases with increasing cluster size. In fact, these activation barriers are similar to the binding energy differences for the removal of single He from clusters (cf., Fig. 2). The corresponding prefactors are fairly standard,

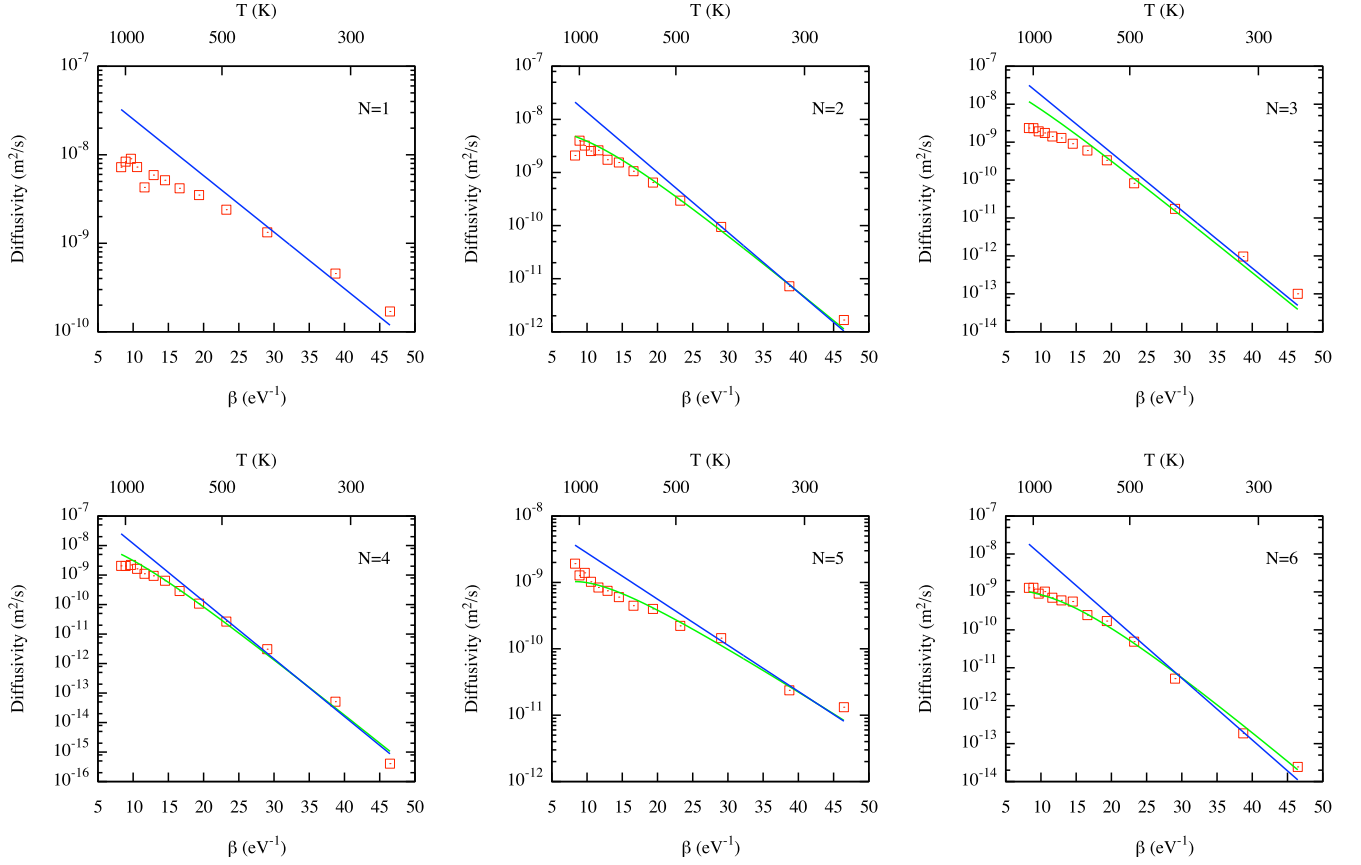


FIG. 8. Diffusivity as a function of  $\beta$  for  $N = 1$  to 6. Red squares: MD results; blue line: HTST; green line: SB-HTST.

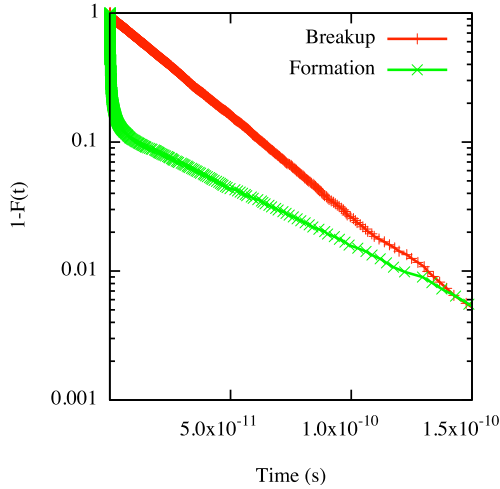


FIG. 9.  $1 - F(t)$  for  $N = 2$  at  $T = 1500$  K with  $R_{\max} = 2.8$  Å. Red: breakup; Green: formation.

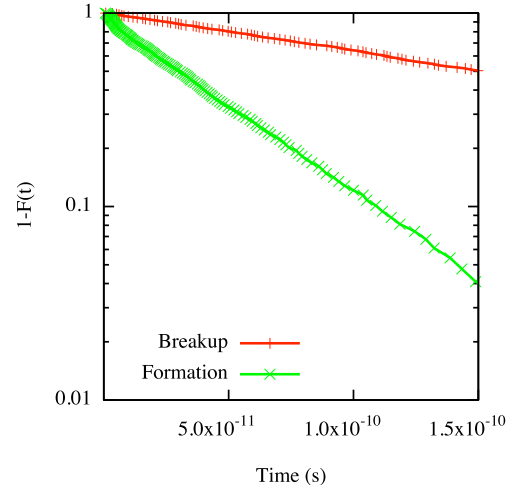


FIG. 10.  $1 - F(t)$  for  $N = 2$  at  $T = 1500$  K with  $R_{\text{bound}} = 2$  Å and  $R_{\text{unbound}} = 7$  Å. Red: breakup; Green: formation.

i.e., around  $10^{12}$  to  $10^{13} \text{ s}^{-1}$ .

Given the very large number of transition pathways (the reverse of every possible clustering pathway), we did

not attempt to exhaustively identify them all in order to perform an SB-HTST correction (as the net effect would result from a competition between the super-basin correc-



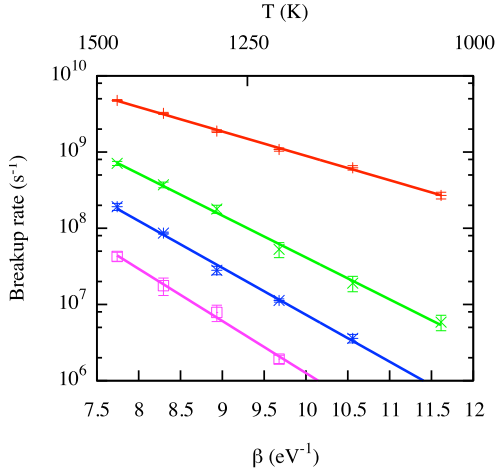


FIG. 11. Breakup rate as a function of  $\beta$ . Red crosses:  $N = 2$ ; Green  $\times$ :  $N = 3$ ; Blue stars:  $N = 4$ ; Pink squares:  $N = 5$ . Corresponding lines are Arrhenius fits.

$N$	$\nu$ ( $s^{-1}$ )	$\Delta E$ (eV)
2	$1.41 \times 10^{12}$	0.74
3	$1.29 \times 10^{13}$	1.27
4	$1.05 \times 10^{13}$	1.41
5	$8.66 \times 10^{12}$	1.57

TABLE II. Prefactors and energy barriers for cluster breakup obtained from an Arrhenius fit to the MD data.

tion and the activation of more pathways). The observed breakup rates are remarkably Arrhenius over the probed temperature range, but deviations at lower temperatures cannot be fully excluded.

While we expect the number of distinct breakup pathways to be large, the vast majority of the breakups involve a single atom leaving the cluster. At elevated temperatures more complex transitions start to activate, but their contribution is modest: at 1500 K, the  $5 \rightarrow 3 + 2$  transition occurs only about 4% of the time, the  $4 \rightarrow 2 + 2$  about 2% of the time. That fraction becomes even more modest at lower temperatures.

### D. Trap Mutation

The last process of interest to microstructural evolution is the so-called “trap mutation” process, whereby an interstitial cluster of He induces the creation of a W Frenkel pair and collapses into the newly created vacancy. From then on, the cluster is practically immobile and can be considered a nano-bubble. Additional He atoms encountering it will also join the bubble, which will grow by further emitting W interstitials<sup>14</sup>. We postpone the analysis of the growth process to a future publication; instead we here assess the rate at which clusters can un-

$N$	$\nu$ ( $s^{-1}$ )	$\Delta E$ (eV)
5	$2.95 \times 10^{12}$	1.20
6	$1.28 \times 10^{13}$	1.02
7	$6.64 \times 10^{12}$	0.701

TABLE III. Prefactors and energy barriers for cluster mutation obtained from an Arrhenius fit to the MD data.

dergo this mutation. The mutation process was observed in direct MD simulations.

A typical mutation event is illustrated in Fig. 12. This process, with an energy barrier of 1.06 eV, was identified from an MD trajectory at 1400 K and characterized using the NEB method. In the initial state, one can clearly see that a W atom was found especially far from its equilibrium configuration [cf., panel a), under the cluster]. As the cluster becomes more compact [cf., panel b)], this atom is further pushed away, which finally leads to its complete ejection [cf., panel c)] and to the formation of an interstitial. After a few rearrangements, the interstitial rearranges into a crowdion configuration (not shown). This process admits many variants (we have identified a selection of these), but the associated barriers appear to be similar to the one described above.

As shown in Fig. 13, the mutation rate increases sharply with size, as expected. At 1000 K, the lifetime of a cluster before mutation varies from a few hundred ns for  $N = 7$  down to a fraction of a  $\mu s$  for  $N = 5$ . Once again, the behavior of the rate is nicely Arrhenius over the range of temperature we investigated (700–1400 K). The results of Arrhenius fits to the MD results are summarized in Table III. The energy barriers extracted from the fits, ranging from 0.701 eV for  $N = 7$  to 1.20 eV for  $N = 5$ , are significantly lower than that of the reaction pathways we found (e.g., 1.06 eV for the  $N = 7$  transition shown in Fig. 12), but the disagreement decreases significantly upon consideration of SB-HTST corrections. For example, for  $N = 7$ , the MD results are consistent with a raw barrier of about 0.9 eV. Based on the slight tendency for under-correction observed in the case of diffusion, it is plausible that a process with a barrier of about 1 eV, as the one described above, fully accounts for the observed results. However, the possibility that lower barrier pathways also contributes to the rate cannot be excluded.

Interestingly, the inverse reaction (the re-absorption of an interstitial) was also observed for  $N = 5$  and 6. The rate for this process is however difficult to determine precisely because the relatively small size of the simulation cell used here might bias the results, as the created interstitial cannot be ejected far away from the cluster due to periodic boundary conditions. Therefore, it remains confined in the vicinity, which artificially increases the recombination rate. We however observe that mutation makes lower energy states accessible for  $N = 7$ , but not for  $N = 5$ , and 6. This is consistent with a higher rate of recombination for smaller clusters.

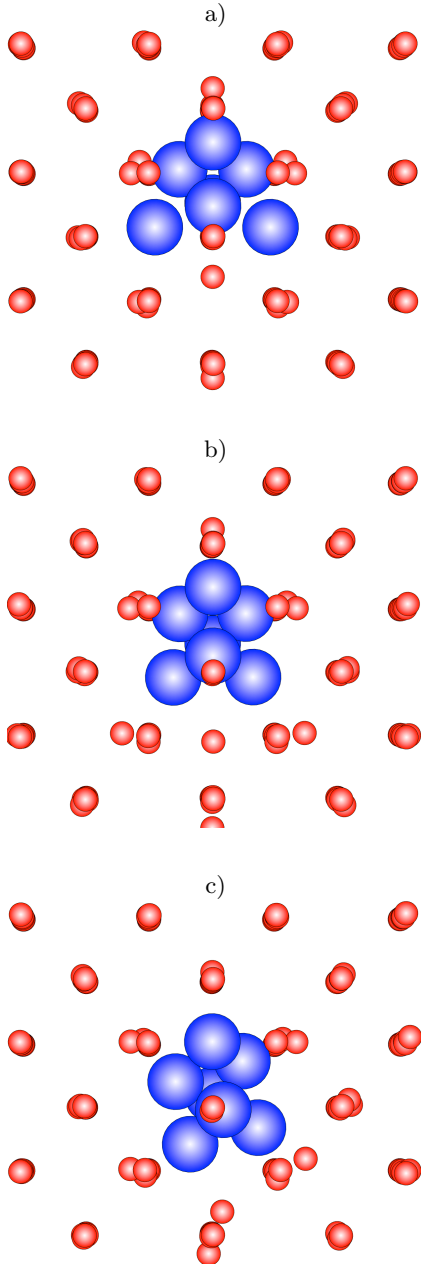


FIG. 12. Possible trap mutation pathway of an  $\text{He}_7$  cluster. The three snapshots correspond to the initial (a), saddle (b), and final (c) configurations.

#### IV. DISCUSSION

The quantities reported above (free energies, diffusivities, breakup rates, and mutation rates) can be used to upscale atomistic simulation through mesoscale cluster dynamics models where the population of individual species is obtained through the solution of a set of coupled reaction/diffusion equations<sup>43</sup>. These models can be used to bridge the gap between the nanoscale and relevant device scales and provide information on the microstructural evolution of the material over long

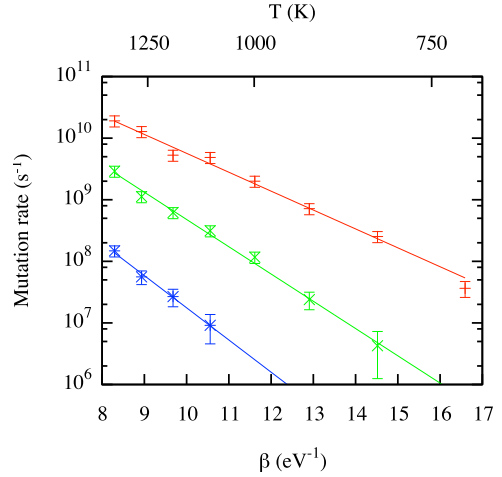


FIG. 13. Mutation rate as a function of  $\beta$ . Red crosses:  $N = 7$ ; Green  $\times$ :  $N = 6$ ; Blue stars:  $N = 5$ . Corresponding lines are Arrhenius fits.

timescale and large lengthscales. In that context, the reaction rates between different species are commonly obtained by assuming diffusion-limited reactions, i.e., that the formation rate constant of a specie  $C$  by collision and merger of two other species  $A$  and  $B$  (He clusters of different sizes in the present context) adopts a Smoluchowski form<sup>59</sup>:

$$k_{A+B \rightarrow C} = 4\pi(D_A + D_B)(r_A + r_B), \quad (6)$$

where the  $D$  are diffusivities and the  $r$  effective capture radii. Using the measured formation rates (of the form  $k_{\text{He}_N + \text{He} \rightarrow \text{He}_{N+1}}$ ), we can extract the relevant capture radii from the atomistic results. We obtain  $r_N \simeq 4.3, 9.9, 15,$  and  $25 \text{ \AA}$  around  $1000 \text{ K}$ , for  $N = 1, 2, 3,$  and  $4$ , respectively, decreasing to about  $r_N \simeq 2.9, 7.3, 9.2,$  and  $13 \text{ \AA}$  around  $1500 \text{ K}$ . These values are surprisingly large compared to an effective hard core radius of a single He atom. This points to a significant contribution from elastic interactions mediated by the tungsten lattice. This is qualitatively consistent with the observation that He atoms bind increasingly strongly with increasing cluster size, even in absence of purely chemical binding between He atoms. This hypothesis can be confirmed directly by calculating the energy of different configurations as a function of the distance between 2 He atoms. For clarity, configurations taken along a trajectory at  $2000 \text{ K}$  have been quenched before computing the distance and potential energy. As shown in Fig. 14, the elastic interaction between a pair of He atoms extends up to a range of about  $6 \text{ \AA}$ . Postulating that capture occurs once the interaction energy reaches about  $k_B T$  yields results that are in reasonable agreement with the radii inferred from Eq. (6).

A commonly taken approach when parameterizing cluster dynamics models is to rely on Eq. (6) combined with a detailed balance condition to estimate the breakup rates of the clusters. This approach is attractive in cases

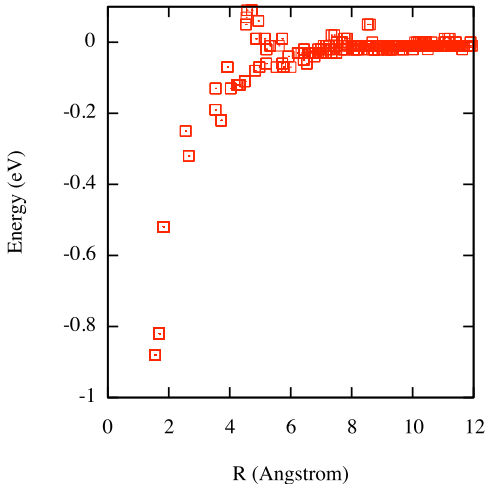


FIG. 14. Potential energy of quenched configurations taken along a 2000 K MD simulation as a function of the distance between 2 He atoms.

where free energy differences are computable using sophisticated sampling techniques and diffusivities and capture radii can be estimated using MD simulations, but where breakup rates are too low to be directly measured. However, as discussed in Sec. III C, a purely thermodynamical description of the breakup process is here inadequate because it leads to non-Markovian breakup kinetics. We next assess whether using the kinetic approach to computing the formation rates and the thermodynamic approach to compute the binding free energy yields accurate results.

Using the free energy change upon breakup  $\Delta F_{C \rightarrow A+B}$ , one gets:

$$k_{C \rightarrow A+B} = \frac{1}{V} k_{A+B \rightarrow C} \exp(-\beta \Delta F_{C \rightarrow A+B}). \quad (7)$$

Using this last equation with the measured formation rates [or, equivalently, using the inferred (temperature-dependent) capture radii] and the calculated binding free energies, the accuracy of this approach can be assessed by comparing to the directly measured breakup rates. As shown in Fig. 15 for the breakup of  $\text{He}_3$ , these two approaches are in close agreement (similar agreement is observed for other reactions). This suggests that, while the absolute values of the formation and breakup rates significantly differ in the thermodynamic and kinetic formalism, their ratio is approximatively the same, i.e., that the correction to the rate can be described using a simple transmission factor.

Our results have some interesting consequences regarding the behavior of He in tungsten. Consider the  $N = 5$  cluster. At  $T = 1000$  K, it has a diffusivity of  $9.14 \times 10^{-10} \text{ m}^2 \text{ s}^{-1}$ , a rate to break-up of  $1.06 \times 10^5 \text{ s}^{-1}$ , and a rate to trap mutate of  $2.64 \times 10^6 \text{ s}^{-1}$ . Thus, the rate to trap mutate is about 20 times that for breaking up at 1000 K and, on the time scale of trap mutation, the cluster can diffuse about 19 nm. In contrast, at 500 K, trap

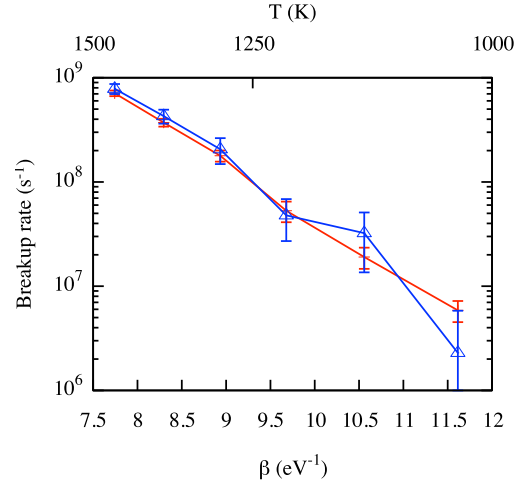


FIG. 15. Breakup rate for the reaction  $\text{He}_3 \rightarrow \text{He}_2 + \text{He}$ . Red: direct MD simulations (cf. Fig. 11); blue: from Eq. (7).

mutation is nearly 2000 times more likely than break-up and the cluster would diffuse over  $10 \mu\text{m}$  before trap mutating. Thus, whether a cluster such as  $N = 5$  would contribute more to the growth or nucleation of bubbles would be very temperature dependent. This has important consequences for the behavior predicted in higher level models and illustrates the need to obtain accurate rates for all relevant processes.

The behavior of these clusters is clearly not a simple function of their size, with particularly the  $N = 5$  cluster exhibiting what might be deemed anomalous behavior as compared with the other clusters. The behavior of the  $N = 5$  cluster is correlated with its structure which, among the clusters examined here, is the sole cluster to contain a He atom in an octahedral position in its ground state. Thus, there is some relationship between, for example, the structure of the cluster and its kinetic properties, though that relationship is not trivial.

Finally, it is interesting to note that, even though these clusters, especially the larger ones, exhibit a very rich and complex landscape of local minima (hundreds of different conformations), their migration rates are very well described by considering them as existing in a super basin that has a key escape pathway. This leads to an excellent description of the migration rates as a function of temperature using SB-HTST. These rates are still harmonic on a basin-to-basin level, but anharmonicity is effectively captured to first order through the fact that the average energy of the minimum is itself a function of temperature. We expect that this modification of harmonic TST will provide a powerful avenue for analyzing the rates of complex structures such as the clusters described here. It should also be very useful in any situation where large regions of configuration spaces are confined by only a few kinetic bottlenecks. In these cases, we would expect the super-basin corrections to be significant. While a brute-force approach to the parameterization of all the inter-



basin rates would be prohibitively expensive, the escape rates out of these bottlenecks can be readily obtained with SB-HTST.

## V. CONCLUSIONS

We investigated the kinetics and thermodynamics of small He clusters in W in conditions relevant to fusion energy production. Our simulations yield insights into the structure and thermodynamics of these clusters, and provide a complete characterization of their kinetics in terms of diffusion, breakup, and mutation into nanoscale He bubbles. Our results enable the parameterization of cluster dynamics models that can bridge the gap between the nano and mesoscales and hence facilitate the prediction of the performance of W as a first-wall material in the next generation of fusion reactors.

## ACKNOWLEDGMENTS

This work was supported by the United States Department of Energy (US DOE) SciDAC program. Los Alamos National Laboratory is operated by Los Alamos National Security, LLC, for the National Nuclear Security administration of the US DOE under contract DE-AC52-06NA25396. This research used resources of the National Energy Research Scientific Computing Center, which is supported by the Office of Science of the U.S. Department of Energy under Contract No. DE-AC02-05CH11231.

## Appendix A: Super-Basin Transition State Theory

Conventional harmonic transition state theory (HTST)<sup>60</sup> is usually appropriate when the initial (reactant) state is composed of a single basin of attraction of the potential energy surface. We now show that it can be generalized in cases where the initial state is a super-basin, i.e., a collection of individual basins. Individual basins can represent different conformations of the same defect, and inter-super-basins transitions can correspond to a net motion of the defect, or to a certain reaction. Assume that the transition path of interest originates in basin  $G$  and leaves the super-basin  $S$  through a dividing surface  $G^*$ . The TST rate  $k$  at which

this transition occurs is simply given by the probability of finding the system in  $G$  relative to elsewhere in the super-basin multiplied by the TST rate for escape from  $G$  across  $G^*$ , i.e.:

$$k = p_G k_{G \rightarrow G^*} = \frac{Z_G}{Z_S} \frac{1}{\beta h} \frac{Z_G^*}{Z_G} = \frac{1}{\beta h} \frac{Z_G^*}{Z_S}, \quad (\text{A1})$$

where the  $Z$  are canonical partition functions.

Computing the slope of the Arrhenius curve at a given inverse temperature  $\beta$ ,

$$\frac{\partial \ln k/k_0}{\partial \beta} = \frac{1}{k} \frac{\partial k}{\partial \beta} \Big|_{\beta}, \quad (\text{A2})$$

where  $k_0$  is an arbitrary constant with the units of a rate. Using Eq. (A1):

$$\frac{\partial \ln k/k_0}{\partial \beta} = \left[ -\frac{1}{\beta} + \frac{1}{Z_G^*} \frac{\partial Z_G^*}{\partial \beta} - \frac{1}{Z_S} \frac{\partial Z_S}{\partial \beta} \right]. \quad (\text{A3})$$

From the fact that  $\partial Z/\partial \beta = \langle -E \rangle_{\beta} Z$ , with  $E$  the total energy, we have:

$$\frac{\partial \ln k/k_0}{\partial \beta} = \left[ -\frac{1}{\beta} + -\langle E \rangle_{G^*, \beta} + \langle E \rangle_{S, \beta} \right]. \quad (\text{A4})$$

In the harmonic approximation, the equipartition theorem holds, and we get:

$$\frac{\partial \ln k/k_0}{\partial \beta} = -[U_G^* - \langle U_{\min} \rangle_{S, \beta}] = -\Delta \tilde{E}(\beta), \quad (\text{A5})$$

where  $U_G^*$  is the potential energy at the saddle point in  $G^*$  and  $\langle U_{\min} \rangle_{S, \beta}$  is the average potential energy of the minimum of the basin the system is currently in. In analogy with conventional Arrhenius kinetics,  $\Delta \tilde{E}(\beta)$  is interpreted as an effective, temperature dependent, activation energy. As the temperature increases, the system will spend increasing amounts of time in higher energy basins, which will lead to a corresponding decrease of the effective activation energy.  $\langle U_{\min} \rangle_{S, \beta}$ , and hence  $\Delta \tilde{E}(\beta)$ , can easily be obtained from direct MD simulations, or estimated by computing harmonic partition functions. Eq. (A5) can then be integrated to give the rate  $k(\beta)$ . Note that in extreme cases one could even observe a *negative* effective activation energy if some local minima in the super-basin are located at energies higher than the saddle  $U_G^*$ .

\* danny\_perez@lanl.gov

<sup>1</sup> G. Janeschitz, J. Nucl. Mater., **290**, 1 (2001).

<sup>2</sup> H. Bolt, V. Barabash, W. Krauss, J. Linke, R. Neu, S. Suzuki, N. Yoshida, and ASDEX Upgrade Team, J. Nucl. Mater., **329**, 66 (2004).

<sup>3</sup> K. Tokunaga, M. J. Baldwin, R. P. Doerner, N. Noda, Y. Kubota, N. Yoshida, T. Sogabe, T. Kato, and

B. Schedler, J. Nucl. Mater., **337**, 887 (2005).

<sup>4</sup> S. Takamura, N. Ohno, D. Nishijima, and S. Kajita, Plasma Fusion Res., **1**, 51 (2006).

<sup>5</sup> M. J. Baldwin and R. P. Doerner, Nucl. Fusion, **48**, 035001 (2008).

<sup>6</sup> M. J. Baldwin, R. P. Doerner, D. Nishijima, K. Tokunaga, and Y. Ueda, J. Nucl. Mater., **390**, 886 (2009).

- <sup>7</sup> D. Nishijima, M.-Y. Ye, N. Ohno, and S. Takamura, *J. Nucl. Mater.*, **329**, 1029 (2004).
- <sup>8</sup> J. Sharpe, D. Petti, and H.-W. Bartels, *Fusion Eng. Design*, **6364**, 153 (2002).
- <sup>9</sup> M. Gilbert, S. Dudarev, S. Zheng, L. Packer, and J.-C. Sublet, *Nuclear Fusion*, **52**, 083019 (2012).
- <sup>10</sup> C. S. Becquart and C. Domain, *Cur. Opin. Solid State Mater. Sci.*, **16**, 115 (2012).
- <sup>11</sup> A. van Veen, L. M. Caspers, E. V. Kornelsen, R. Fastenau, A. van Gorkum, and A. Warnaar, *Phys. Status Solidi A*, **40**, 235 (1977).
- <sup>12</sup> W. Wilson, C. Bisson, and M. Baskes, *Phys. Rev. B*, **24**, 5616 (1981).
- <sup>13</sup> A. S. Parasnis, J. W. Mitchell, and H. H. Wills, *Philos. Mag.*, **4**, 171 (1959).
- <sup>14</sup> G. W. Greenwood, A. J. E. Foreman, and D. E. Rimmer, *J. Nucl. Mater.*, **1**, 305 (1959).
- <sup>15</sup> M. I. Baskes, R. H. J. Fastenau, P. Penning, L. M. Caspers, and A. van Veen, *J. Nucl. Mater.*, **102**, 235 (1981).
- <sup>16</sup> M. Baskes and W. Wilson, *Phys. Rev. B*, **27**, 2210 (1983).
- <sup>17</sup> J. H. Evans, A. van Veen, and L. M. Caspers, *Scripta Metall.*, **15**, 323 (1981).
- <sup>18</sup> E. V. Kornelsen and A. A. Van Gorkum, *J. Nucl. Mater.*, **92**, 79 (1980).
- <sup>19</sup> M. Puska and R. Nieminen, *Phys. Rev. B*, **29**, 5382 (1984).
- <sup>20</sup> H. Iwakiri, K. Yasunaga, K. Morishita, and N. Yoshida, *J. Nucl. Mater.*, **283**, 1134 (2000).
- <sup>21</sup> P. E. Lhuillier, T. Belhabib, P. Desgardin, B. Courtois, T. Sauvage, M. F. Barthe, A. L. Thomann, P. Brault, and Y. Tessier, *J. Nucl. Mater.*, **433**, 305 (2013).
- <sup>22</sup> L. M. Caspers, R. H. J. Fastenau, A. van Veen, and W. F. W. M. van Heugten, *Phys. Status Solidi A*, **46**, 541 (1978).
- <sup>23</sup> M. Abd El Keriem, D. van der Werf, and F. Pleiter, *Phys. Rev. B*, **47**, 14771 (1993).
- <sup>24</sup> C. S. Becquart and C. Domain, *Nucl. Instrum. Methods Phys. Res. B*, **255**, 23 (2007).
- <sup>25</sup> J. X. Yan, Z. X. Tian, W. Xiao, and W. T. Geng, *J. Appl. Phys.*, **110**, 013508 (2011).
- <sup>26</sup> W. Hao and W. T. Geng, *Nucl. Instrum. Methods Phys. Res. B*, **280**, 22 (2012).
- <sup>27</sup> T. Seletskaiia, Y. N. Osetsky, R. E. Stoller, and G. M. Stocks, *J. Nucl. Mater.*, **351**, 109 (2006).
- <sup>28</sup> D. M. Stewart, Y. N. Osetsky, R. E. Stoller, S. I. Golubov, T. Seletskaiia, and P. J. Kamenski, *Philos. Mag.*, **90**, 935 (2010).
- <sup>29</sup> D. Stewart, Y. Osetskiy, and R. Stoller, *J. Nucl. Mater.*, **417**, 1110 (2011).
- <sup>30</sup> L. Yang, H. Q. Deng, F. Gao, H. L. Heinisch, R. J. Kurtz, S. Y. Hu, Y. L. Li, and X. T. Zu, *Nucl. Instrum. Methods Phys. Res. B*, **303**, 68 (2013).
- <sup>31</sup> K. O. E. Henriksson, K. Nordlund, and J. Keinonen, *Nucl. Instrum. Methods Phys. Res. B*, **244**, 377 (2006).
- <sup>32</sup> F. Sefta, K. D. Hammond, N. Juslin, and B. D. Wirth, *Nucl. Fusion*, **53**, 073015 (2013).
- <sup>33</sup> A. Caro, J. Hetherly, A. Stukowski, M. Caro, E. Martinez, S. Srivilliputhur, L. Zepeda-Ruiz, and M. Nastasi, *J. Nucl. Mater.*, **418**, 261 (2011).
- <sup>34</sup> N. Gao, H. Van Swygenhoven, M. Victoria, and J. Chen, *J. Phys. Condens. Matter*, **23**, 442201 (2011).
- <sup>35</sup> Y. F. Zhang, P. C. Millett, and M. Tonks, *Comput. Mater. Sci.*, **50**, 3224 (2011).
- <sup>36</sup> J. Boisse, C. Domain, and C. Becquart, *Journal of Nuclear Materials*, **455**, 10 (2014), ISSN 0022-3115, proceedings of the 16th International Conference on Fusion Reactor Materials (ICFRM-16) Proceedings of the 16th International Conference on Fusion Reactor Materials (ICFRM-16), Beijing, China, 20th - 26th October, 2013.
- <sup>37</sup> E. Hayward and C. Deo, *J. Phys. Condens. Matter*, **24**, 265402 (2012).
- <sup>38</sup> H. Trinkaus, *Radiat. Eff.*, **78**, 189 (1982).
- <sup>39</sup> K. Morishita, *Philos. Mag.*, **87**, 1139 (2007).
- <sup>40</sup> C. S. Becquart, C. Domain, U. Sarkar, A. DeBacker, and M. Hou, *J. Nucl. Mater.*, **403**, 75 (2010).
- <sup>41</sup> X. Guo, X. Zhang, J. Xue, and W. Li, *Nucl. Instrum. Methods Phys. Res. B*, **307**, 77 (2013).
- <sup>42</sup> D. H. Xu and B. D. Wirth, *J. Nucl. Mater.*, **403**, 184 (2010).
- <sup>43</sup> J. Marian and T. L. Hoang, *J. Nucl. Mater.*, **429**, 293 (2012).
- <sup>44</sup> L. Hu, K. D. Hammond, B. D. Wirth, and D. Maroudas, *Surface Science*, **626**, L21 (2014), ISSN 0039-6028.
- <sup>45</sup> M. R. Sørensen and A. F. Voter, *J. Chem. Phys.*, **112**, 9599 (2000).
- <sup>46</sup> J. Kim, J. E. Straub, and T. Keyes, *Phys. Rev. Lett.*, **97**, 050601 (2006).
- <sup>47</sup> U. H. E. Hansmann, Y. Okamoto, and F. Eisenmenger, *Chem. Phys. Lett.*, **259**, 321 (1996).
- <sup>48</sup> C. Junghans, D. Perez, and T. Vogel, *J. Chem. Theory Comput.*, **10**, 1843 (2014).
- <sup>49</sup> D. Perez, B. P. Uberuaga, Y. Shim, J. G. Amar, and A. F. Voter, in *Annual Reports in Computational Chemistry*, Vol. 5, edited by R. A. Wheeler (Elsevier, 2009) pp. 79–98.
- <sup>50</sup> G. Henkelman, B. P. Uberuaga, and H. Jónsson, *J. Chem. Phys.*, **113**, 9901 (2000).
- <sup>51</sup> G. J. Ackland and R. Thetford, *Philos. Mag. A*, **56**, 15 (1987).
- <sup>52</sup> N. Juslin and B. D. Wirth, *J. Nucl. Mater.*, **432**, 61 (2013).
- <sup>53</sup> D. E. Beck, *Mol. Phys.*, **14**, 311 (1968); **15**, 332 (1968).
- <sup>54</sup> K. Morishita, R. Sugano, B. D. Wirth, and T. Diaz de la Rubia, *Nucl. Instrum. Methods Phys. Res. B*, **202**, 76 (2003).
- <sup>55</sup> G. Szabó, *J. Phys. C: Solid State Phys.*, **19**, 3775 (1986).
- <sup>56</sup> J. T. Kindt, *J. Chem. Theory Comput. (JCTC)*, **9**, 147 (2013).
- <sup>57</sup> D. Simonovic, C. K. Ande, A. I. Duff, F. Syahputra, and M. H. F. Sluiter, *Phys. Rev. B*, **81**, 054116 (2010).
- <sup>58</sup> E. Vanden-Eijnden and F. A. Tal, *J. Chem. Phys.*, **123**, 184103 (2005).
- <sup>59</sup> M. V. Smoluchowski, *Z. Phys. Chem.*, **92**, 129 (1917).
- <sup>60</sup> G. H. Vineyard, *J. Phys. Chem. Solids*, **3**, 121 (1957).